



Inhibition of SUMOylation Induces Adaptive Antitumor Immunity against Pancreatic Cancer through Multiple Effects on the Tumor Microenvironment

Suna Erdem¹, Hyojae James Lee¹, Jayanth Surya Narayanan Shankara Narayanan¹, Mohottige Don Naranjan Tharuka¹, Jorge De la Torre², Tianchen Ren^{3,4}, Yixuan Kuang^{3,4}, Tharindumala Abeywardana¹, Kevin Li², Allison J. Berger⁵, Andrew M. Lowy^{1,2}, Rebekah R. White^{1,2}, and Yuan Chen^{1,3}

ABSTRACT

Improvement of outcome in patients with pancreatic ductal adenocarcinoma (PDAC) requires exploration of novel therapeutic targets. Thus far, most studies of PDAC therapies, including those inhibiting small ubiquitin-like modifications (SUMOylation), have focused on PDAC epithelial cell biology, yet SUMOylation occurs in a variety of cell types. The mechanisms by which SUMOylation impacts PDAC in the context of its tumor microenvironment are poorly understood. We used clinically relevant orthotopic PDAC mouse models to investigate the effect of SUMOylation inhibition using a specific, clinical-stage compound, TAK-981. In contrast to its inhibition of PDAC cell proliferation *in vitro*, the survival benefit conferred by TAK-981 *in vivo* is dependent on the presence of T cells, suggesting that induction of adaptive antitumor

immunity is an important antitumor effect of SUMOylation inhibition *in vivo*. To understand how this adaptive antitumor immunity is promoted, we investigated how SUMOylation inhibition *in vivo* alters major cell types/subtypes and their communications in the PDAC tumor microenvironment by performing transcriptomic analyses at single-cell resolution, which allowed mapping of cells in our orthotopic mouse model to cells in human PDAC tumors based on gene expression profiles. Findings are further validated by flow cytometry, immunofluorescence, IHC, western blots, and qPCR. The single-cell transcriptome dataset provided here suggests several combination strategies to augment adaptive immune responses that are necessary for durable disease control in patients with PDAC.

Introduction

Pancreatic ductal adenocarcinoma (PDAC) is a highly lethal malignancy with a 5-year overall survival rate of approximately (1) 13%. Various cytotoxic chemotherapeutic combinations have improved the median survival of patients with metastatic disease by only a few months (2), and there is considerable associated toxicity. Immunotherapies have produced a paradigm shift in the treatment of several cancers by generating durable remissions not achieved with chemotherapy or targeted therapy alone. Unfortunately, these therapies have not shown similar benefit in PDAC (3, 4). Thus, it is important to investigate novel mechanisms to advance PDAC therapy.

Many previous studies have suggested that small ubiquitin-like modification (SUMOylation) is a rational therapeutic target for

PDAC therapy. The SUMO family has four members (SUMO-1, SUMO-2, SUMO-3, and SUMO-4) that are ubiquitin homologs and can be catalyzed to form covalent bonds with other proteins through a mechanism analogous to ubiquitination. SUMOylation requires several steps that are catalyzed by three enzymes: E1, the SUMO activating enzyme (SAE), which is a heterodimer of SAE1 and SAE2 (also known as UBA2); E2, the conjugation enzyme, also known as Ubc9 (also known as UBE2I); and one of ~10 E3 ligases. There is a single E1 and E2 enzyme for all SUMO paralogs. SUMO modification adds a new docking site to target proteins and thus enables signaling and/or modifies protein complex formation through the SUMO-interacting motif in receptor proteins (5, 6). Several previous studies have suggested that inhibition of SUMOylation inhibits cell cycle progression (7–9) and Myc- and KRas-dependent oncogenesis (8, 10), which are major oncogenic drivers of PDAC.

Studies of PDAC therapies thus far, including SUMOylation inhibition, have focused on PDAC epithelial cell biology. However, it has been shown that cell state, plasticity, and drug resistance of PDAC are strongly impacted by the tumor microenvironment (TME) because of cell-cell communications mediated by direct receptor-ligand interactions or indirectly through secreted cytokines and other factors (11). SUMOylation occurs in all cell types and thus it is unclear how the TME may impact PDAC cell responses to SUMOylation inhibition. The first-in-class SAE inhibitor subsumstat (TAK-981) has been evaluated in Phase 1/2 clinical trials (12–14). Therefore, preclinical studies of TAK-981 in PDAC could provide the rationale to further study this approach in patients with PDAC.

In this study, we investigated how inhibiting SUMOylation with TAK-981 would impact PDAC using orthotopic PDAC mouse

¹Moores Cancer Center, UC San Diego, La Jolla, California. ²Division of Surgical Oncology, Department of Surgery, UC San Diego, La Jolla, California. ³Division of Surgical Sciences, Department of Surgery, UC San Diego, La Jolla, California. ⁴Graduate Program in Chemistry and Biochemistry, UC San Diego, La Jolla, California. ⁵Takeda Development Center Americas Inc., Lexington, Massachusetts.

S. Erdem, H.J. Lee, and J.S.N. Shankara Narayanan contributed equally to this article.

Corresponding Authors: Yuan Chen, Moores Cancer Center, UC San Diego, 3855 Health Sciences Drive, La Jolla, CA 92037. E-mail: yuc020@ucsd.edu; and Rebekah R. White, rewhite@health.ucsd.edu

Mol Cancer Ther 2024;23:1597–612

doi: 10.1158/1535-7163.MCT-23-0572

©2024 American Association for Cancer Research

models and through comparative analyses with human PDAC at single-cell resolution. One of our mouse models recapitulates human PDAC in that it readily metastasizes to the liver, which is the main site of PDAC metastasis, and that it forms a TME containing nearly all cell types found in human PDAC, including normal ductal cells, pancreatic stellate cells, tumor-associated macrophages (TAM), cancer-associated fibroblasts (CAF), endothelial cells, and T and NK cells. TAK-981 treatment of orthotopic PDAC tumors significantly increased survival in wild-type mice. Unexpectedly, the survival benefit is lost in *Rag1^{-/-}* mice, despite strong inhibition of TAK-981 on tumor cell proliferation *in vitro*. This suggests that *in vivo*, the more impact of SAE inhibition is to induce antitumor T-cell responses than to directly inhibit tumor cell growth. To understand how this adaptive antitumor immunity is promoted, we investigated how SAE inhibition *in vivo* alters major cell types/subtypes and their communications in the PDAC TME by performing transcriptomic analyses at single-cell resolution in combination with other approaches. We found that, in addition to enhancing T-cell activation and tumor infiltration (12), TAK-981 promoted T-cell differentiation into effector and memory phenotypes and reduced the expression of some exhaustion markers in the TME. Comparative single-cell transcriptomics analyses of human and mouse PDAC tumors supported a direct role for SUMOylation in regulating T-cell differentiation, memory formation, and exhaustion. SAE inhibition also modulated TAM subtypes and their gene expression and reduced CAF interactions with other cells in the TME, which likely promoted antitumor T-cell responses. Our findings demonstrate that SAE inhibition induces antitumor T-cell responses through effects on multiple cells in the TME. These findings, including cross-species gene expression analyses at single-cell resolution, form the basis for developing future combination strategies to achieve durable treatment responses in PDAC and potentially other cancers with a similar TME.

Materials and Methods

Isg15 western blot

Mouse splenocyte lysates from KPC tumor-bearing mice treated with TAK-981 or vehicle control were prepared by sonication with SDS loading buffer (1X) including 1% β-mercaptoethanol. Samples were run in MES SDS running buffer (1X, Cat. # NP0002, Life Technologies, USA) and transferred to nitrocellulose membranes (0.45 μm; Cat. # LC2001, Invitrogen, USA) in transfer buffer (NuPAGE transfer buffer, 1X, NP0006-1, 20% methanol). Ponceau staining of the gels was used as confirmation of equal protein loading. Isg15 was detected using 0.5 μg/mL of the primary antibody, as previously described (15).

TAK-981

TAK-981 used in the study was provided by Takeda Development Center Americas, Inc. or purchased from Chemietek (Catalog number: CT-TAK981). TAK-981 purchased from Chemietek was verified by nuclear magnetic resonance and LC-MS and by enzymatic inhibition assay.

RNA isolation, cDNA preparation, and quantitative real-time PCR

Tumors were collected and RNA was purified from the tumor lysates. An amount of 1 μg from each RNA sample was used for cDNA synthesis (iScript CDNA synthesis Kit, Cat. # 1708890, Bio-Rad, USA). Q-PCR reactions were performed using 1 μL of diluted

cDNA (1:20) as template, 0.3 μL of each forward and reverse gene-specific primers (10 pmol/μL), 5 μL of PowerUp SYBR Green Master Mix, Cat. # A25742 (Applied biosystems, USA) and 2.4 μL of nuclease-free H₂O. Expressions were analyzed as previously described (16).

Organoid culture

KPC-46-1 organoids were developed from a male *Kras^{LSL-G12D}-p53^{LSL-R172H}-Pdx-1-Cre* (KPC) mouse bearing pancreatic carcinoma using the protocol described in ref. 17. The cell line was authenticated by sequencing and confirmed negative for pathogens using IMPACT testing (IDEXX Bioresearch). In short, ~300 to 500 mg of primary tumor tissue were washed in PBS, minced into small pieces and added to 4.7-mL RPMI with 1-mg/mL collagenase and dispase, and incubated for 1 hour at 37°C. The enzymes were then removed by centrifugation and the cells were placed in a 12-well tissue culture dish at a density of 100,000 to 200,000 cells per 50 μL of growth factor-reduced Matrigel (Corning, #354320) with 800 μL of growth media containing RPMI, 5% FBS, 2× P + S, 1-mmol/L Glutamax, 1-mmol/L sodium pyruvate, 1X nonessential amino acids (NEAA), 1X Fungizone, 5-μg/mL insulin, 1.4-μmol/L hydrocortisone, 10-nM EGF, 10.5-μmol/L rho kinase inhibitor.

Establishment of orthotopic organoid mouse model

All mouse model studies described in this manuscript have been approved by the Institutional Animal Care and Use Committee. Matrigel domes containing the organoids were dislodged from the culture dish and resuspended in 25 mL of cold media. The organoids were then sheared out of the Matrigel scaffold using 23 G needles to establish single organoid suspensions. A small portion of the suspension (1–2 mL depending on the extent of organoid growth) was retrieved, and centrifuged at 2,000 RPM for 15 minutes. To the pellet, 1 mL of TryPLExpress cell dissociation reagent was added and was incubated for 1 hour at 37°C to achieve a single-cell suspension. A cell count was performed on this suspension to establish the total number of cells in the remaining organoid suspension. The suspension containing the organoids was then centrifuged at 2,000 RPM for 15 minutes at 4°C. Supernatant was discarded carefully without disrupting the pellet, and the organoids were resuspended in 100% growth factor-depleted Matrigel at a density of 2.5 million cells/mL. The surgical procedure for pancreas access and tumor implantation to the pancreas was described previously (18). In short, under inhaled isoflurane (2% in 3-L/min oxygen carrier gas) general anesthesia, 20 μL of organoids suspended in Matrigel were injected into the pancreatic tail of 8-week-old male B6/129 F1 mice through a posterior subcostal incision. Mice were administered 1 mg/kg buprenorphine before the completion of the implantation procedure. The tumors were allowed to grow for 14 to 21 days and were monitored using handheld ultrasound imaging (SonoQue L5P). All interventions were performed upon detection of a measurable orthotopic tumor 3 to 4 mm in diameter. This model was established in B6129SF1/J (Jackson Laboratory, # 101043) or B6.129S7-Rag1tm1Mom/J (Jackson Laboratory, # 002216).

The KPC4580P model was established by subcutaneous donor tumors, which were then cut into pieces to be transplanted into the tails of the pancreas of immunocompetent C57Bl6 mice as we previously described (19, 20). The cell line was obtained as previously described (21). The cell line was negative for mycoplasma and several mouse pathogens by Comprehensive IMPACT II testing (IDEXX Bioresearch). Cells were used within three passages of being

thawed from frozen aliquots of the tested stock for every experiment but were not reauthenticated in the past year.

IHC and IF staining

Tissue sections of five-micron thickness were baked at 60°C for 1 hour and were cleared and rehydrated through successive alcohol immersion ($3 \times$ Xylene, $2 \times$ 100% EtOH, $2 \times$ 95% EtOH, $2 \times$ 70% EtOH, diH₂O). Antigen retrieval was performed in Antigen Unmasking Solution (Citrate Based, pH6; Vector, H-3300) at 95°C for 30 minutes. IHC staining was performed on Intellipath Automated IHC Stainer (Biocare) with the following antibodies: anti-SUMO2/3/4 Primary Antibody (Rabbit, Abcam, ab109196, 1:100), Anti-Desmin Primary Antibody (Goat, Santa Cruz, sc-7559, 1:100), or Anti-CD31 Primary Antibody (Rabbit, Abcam, ab28364, 1:50) for 1 hour. The slides were washed with $2 \times$ TBS with 0.1% Tween-20 (TBST) and incubated in a secondary antibody, anti-Rat HRP Polymer (Cell IDX, 2AH-100), for 30 minutes. The tissues were washed $2 \times$ in TBST and developed with DAB (brown) Chromogen (VWR, 95041-478) for 5 minutes and washed again $2 \times$ in deionized H₂O.

Immunofluorescence (IF) staining was performed on Intellipath Automated IHC Stainer (Biocare), with the following steps. Peroxidase block with Bloxall (Vector, SP-6000) for 10 minutes followed by $2 \times$ wash in TBST and blocking with 3% Donkey Serum for 10 minutes. Anti-FOXP3 primary antibody (Rat, Invitrogen, 14-5773-82, 1:200) for 1 hour. The slides were washed with $2 \times$ TBST and incubated in a secondary antibody, anti-Rat HRP Polymer (Cell IDX, 2AH-100), for 30 minutes. The tissues were washed $2 \times$ in TBST and developed using Tyramide-647 Reagent (Thermo, B40953) for 10 minutes and washed again $2 \times$ in deionized H₂O. The same steps from antigen retrieval to development were repeated for each of the primary–secondary antibodies [Anti-CD4 (Rabbit, Abcam, ab183685, 1:100)—Tyramide 488; Anti-CD8 (Rat, Invitrogen, 14-0195-82)—Tyramide 555; Anti-TIM3 (Rabbit, Abcam, EPR22241)—Tyramide 790; Anti-CD3 Primary Antibody (Rabbit, Abcam, ab16669, 1:100)—Tyramide 488; Anti-PDL1 (Rabbit, Cell Signaling, 13684S, 1:100)—Tyramide 555]. Tissues were counterstained with 4',6-diamidino-2-phenylindole (DAPI; 1 µg/mL) for 15 minutes and mounted onto coverslip with Vectashield Vibrance/w DAPI (Vector, H-1800-10).

The slides were imaged using a Zeiss Axio Scan Z1 slide scanner enabled with a high-efficiency filter set for multiplex fluorescence imaging, with a 20× objective and the numerical aperture set at 0.8. Whole slide images were analyzed using QuPath 3.0 software. The individual fluorescence channels were set at the following thresholds: DAPI—(17280–32127); CD4—488 (2249–14404); CD8—555 (330–7451); FoxP3—647 (192–1033); and TIM3—790 (4856–8068). Cell detection was performed using the DAPI-nucleus channel. A single measurement classifier was used to define positive cells on each channel, and a sequential object classification module was performed to detect individual cells positive for individual as well as multiple specific markers.

KPC-46-1 tumor dissociation and single-cell preparation

KPC tumors were isolated from four mice, two treated with TAK-981 and two control mice. Tumors were dissociated using the mouse Tumor Dissociation Kit (Miltenyi) and the gentleMACS Octo Dissociator (Miltenyi), followed by 70-µm cell strainer filtering with 10 mL of cell wash buffer (1× PBS + 0.04% BSA) and centrifugation at 300 relative centrifugal force (rcf) for 5 minutes at room temperature. The pellets were treated with 1-mL ACK lysing buffer

(Gibco) for 1 minute, diluted with 10-mL wash buffer, centrifuged at 300 rcf for 5 minutes at 4°C, and resuspended with 10- to 15-mL wash buffer (aiming for 1,500 cells/µL). Cells were counted using Thermo Fisher Countess 3 Cell Counter and 10,000 to 20,000 total live cells were prepared for each sample. For cells with less than 70% viability, dead cell removal was performed with an aim for >80% viability for all samples using the Dead Cell Removal Kit (Miltenyi).

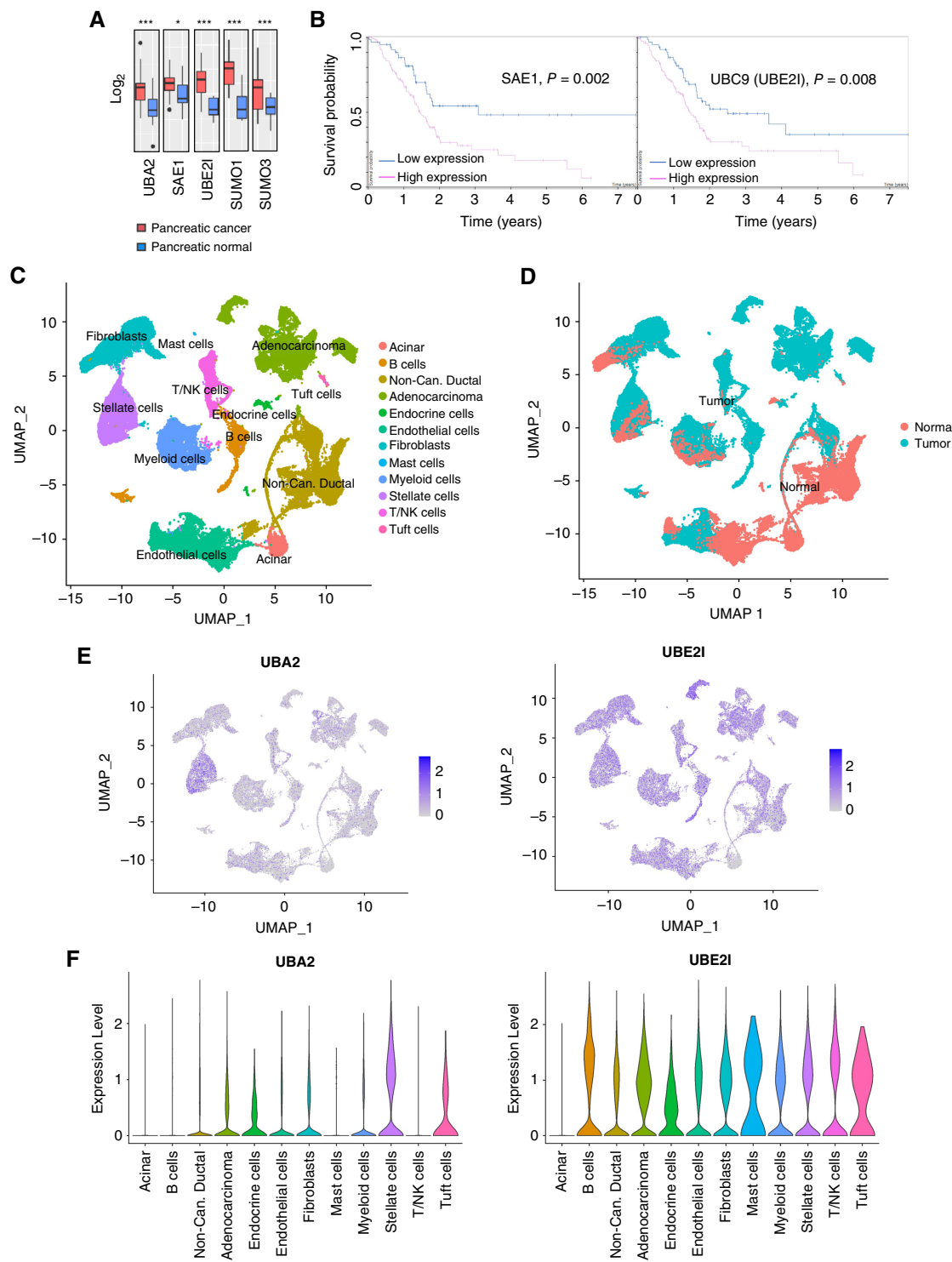
Single-cell RNA sequencing of KPC-46-1 tumors and data processing

For single-cell library construction for KPC-46-1 mouse tumors established in WT mice, 10,000 to 20,000 cells from each sample were used along with Chromium Next GEM Single Cell 3' v3.1 (dual index) and Chromium controller, both from 10× Genomics. Libraries were sequenced on an Illumina NovaSeq 6000 S4 at 200 mol/L reads per sample. The FASTQ files for the control samples were then processed further using seqtk to randomly subsample 55,000,000 read pairs, which resulted in a similar number of cells across all samples for the downstream analysis. The FASTQ files then went through unique molecular identifier (UMI) quantification for which 10× CellRanger v6.1.2 was run on an Amazon Web Service (AWS) EC2 instance (r6i.16xlarge with 64 vCPU, 512 GiB memory). The reads were aligned to the mm10 reference genome.

Quality control and nonlinear dimensionality reduction

Once the filtered count matrices were created, the Seurat package (v4.1.0) was used for the downstream analyses. Each sample object was filtered by the following criteria: cells with between 200 to 10,000 genes, 1,000 to 40,000 UMIs, less than 25% of mitochondrial genes, and less than 40% of ribosomal genes. After creating a list of the Seurat objects, the SCTtransform function was performed. UMI counts, mitochondrial genes, and ribosomal genes were regressed during the transformation. The normalized data were integrated using 3,000 anchor features. Principal component analysis (PCA) was performed on the integrated data as well as t-distributed stochastic neighbor embedding (t-SNE) and Uniform Manifold Approximation and Projection for Dimension Reduction (UMAP) calculation, shared nearest-neighbor graph construction using FindNeighbors, and FindClusters, which performs cluster determination using the shared nearest-neighbor graph modularity optimization-based clustering algorithm (all using 40 dimensions, with resolution = 1.0).

After clustering using SCTtransform, log normalization with a scale factor of 10,000 was performed separately followed by data scaling. Cluster marker sets were calculated using the FindAllMarkers function with its default nonparametric Wilcoxon rank sum test (parameters used: only positive markers, fraction of expression cells inside the cluster ≥ 0.25 , and log fold change between cells inside and outside the cluster ≥ 0.25). All cluster marker genes were saved as tables (Supplementary Tables S1 and S2). Immune cells and nonimmune cells were separated using Ptprc (CD45) expression levels. These separate objects went through the same workflow as above for better cluster identification. The top 10 expressed genes per cluster were plotted on heatmaps (Supplementary Fig. S1). For gene set enrichment analysis (GSEA), FGSEA (v1.20.0) and hallmark gene sets v7.5.1 (Broad Institute) were used. To perform permutation tests for cell type proportion changes, scProportionTest (22) was used.

**Figure 1.**

Analysis of single-cell transcriptomics of human samples shows broad elevated expression of SUMOylation-related genes in ductal tumor cells, CAFs, myeloid cells, and other cell types in the TME. **A**, Log₂ expression levels of SUMOylation-related genes in normal pancreas versus pancreatic cancer using the database GENT2 (25). **B**, Kaplan-Meier curves showing the survival probability differences between groups with either high or low expression levels of SAE1 or UBC9 obtained using the Human Protein Atlas database. **C**, UMAP visualization plot of PCA on all cells from human patient data including 24 PDAC patient tumors and 11 non-PDAC human pancreas tissues (23). The cells are grouped into specific cell types. **D**, UMAP visualization plot of PCA on all cells from the same human samples as in **C**. The cells are categorized as “normal” or “tumor” based on the origins of the cells. **E**, Feature plots of essential SUMOylation-related genes, UBA2 and UBE2I (UBC9), in the samples shown in **C**. **F**, Violin plots of the SUMOylation-related genes in the same samples shown in **C** and **E**.

Single-cell RNA-seq analysis of human PDAC data

Human patient PDAC single-cell RNA sequencing (RNA-seq) data were obtained from Peng and colleagues (GSA: CRA001160; ref. 23). The data consist of 35 patient samples, three of which are obtained from nonpancreatic tumor patients, eight of which are obtained from nonmalignant pancreatic tumor patients, and 24 of which were obtained from patients with PDAC.

The count matrix was imported using R and Seurat package (v4.1.0). The Seurat object was then normalized using the SCTtransform function (regularized negative binomial regression) instead of the traditional log normalization in order to recover better biological distinction (24). Consequently, RunPCA, RunUMAP, FindNeighbors, and FindClusters were used with dimension values of 1:40 and a resolution of 0.4 for the latter function. Once the clustering was done, the regular log normalization was applied to the "RNA" assay along with ScaleData on all genes in order to find marker genes for each cluster. Cluster marker sets were calculated using the FindAllMarkers function with its default non-parametric Wilcoxon rank sum test (parameters used: only positive markers, fraction of expression cells inside the cluster ≥ 0.25 , log fold change between cells inside and outside the cluster ≥ 0.25). All cluster marker genes were saved as tables (Supplementary Table S1).

Data availability

Both the raw and processed single-cell RNA-seq data of mouse KPC-46-1 tumors have been deposited on the NCBI Gene Expression Omnibus with accession ID of GSE212446.

Results

Analysis of human PDAC single-cell datasets suggests important roles of SUMOylation in both cancer cells and stromal cells

Analysis of bulk gene expression datasets using the GENT2 program (25) revealed higher expression of SUMOylation-related genes in PDAC tumor tissues than in noncancerous pancreatic tissues (Fig. 1A). In addition, higher expression of the genes critical for SUMOylation, such as the activating enzyme (SAE) subunit SAE1 and the E2 enzyme UBE2I, correlated with worse survival, based on data from the Human Protein Atlas (Fig. 1B). These analyses suggest that the upregulation of genes essential for SUMOylation activities in PDAC tumors may support disease progression.

To investigate which cell types in PDAC tumors have upregulated SUMOylation-related gene expression, we analyzed a previously published single-cell RNA-seq dataset from 24 PDAC tumor samples and 11 noncancerous pancreatic tissue samples, containing a total of 41,986 cells from PDAC samples and 15,544 cells from noncancerous samples (23). The cells were classified into different cell types (noncancerous ductal, adenocarcinoma, acinar, endocrine, endothelial, fibroblast, stellate, macrophage, T, NK, and B cells) based on gene expression profiles (Fig. 1C; Supplementary Fig. S1A; Supplementary Table S1). The origins of the cells, from tumor and nontumor samples, are indicated in Fig. 1D.

We found that genes related to SUMOylation are expressed in all cell types but they are expressed at a higher level in adenocarcinoma cells than noncancerous ductal cells (Fig. 1E and F). A cluster of tumor cells showed higher levels of UBE2I than other tumor cell clusters, and their top expressed genes are listed in Supplementary Fig. S1C. In addition, pancreatic stellate cells, which are myofibroblast-like cells, and fibroblasts have large tumor-specific

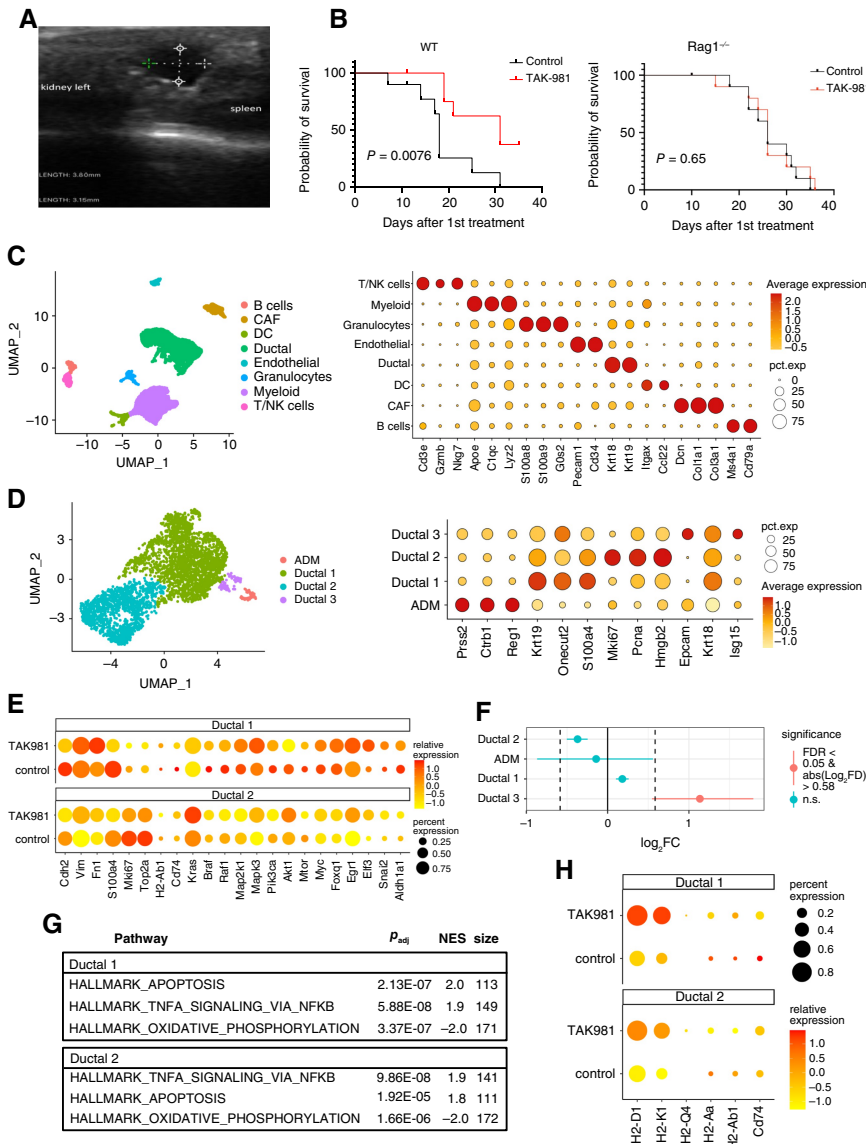
populations and express elevated levels of the essential SUMOylation gene UBA2 relative to other cell types. A similar trend was observed in another single-cell dataset of human PDAC tumors (Supplementary Fig. S1D and S1E; ref. 26). These findings suggest that SUMOylation inhibition could impact both immune and nonimmune stromal cells in addition to cancer cells in PDAC tumors.

An orthotopic mouse model recapitulates the TME of human PDAC, and inhibition of SUMOylation increases survival in a T cell-dependent manner

To investigate the effect of SAE inhibition on PDAC, we carried out studies using two different immunocompetent, orthotopic models using cell or organoid lines derived from the LSL-KrasG12D/+;LSL-Trp53R172H/+;Pdx-1-Cre (KPC) genetic model (27). One model used a cell line (KPC4580P; ref. 21) to initiate orthotopic tumors in the tails of the pancreas of immunocompetent C57Bl6 mice as we previously described (19, 20). Another model is a 3D organoid line (KPC-46-1) derived from a liver metastatic tumor of the KPC genetic model (27). For this model, when cells are injected orthotopically into the pancreatic tail, resultant tumors readily metastasize to the liver, the main site of PDAC metastasis (Supplementary Fig. S2A).

Tumors were assessed through ultrasound imaging (Fig. 2A) and at the end of treatment (Supplementary Fig. S2B), and animals were randomized to treatment groups when tumors reached 3 to 4 mm in diameter. The SUMOylation inhibitor, TAK-981, was dosed at 15 mg/kg every 48 hours. The dose and frequency were determined based on achieving SUMOylation inhibition as observed by IHC staining (Supplementary Fig. S2C), and by inducing type I IFN response in peripheral blood (Supplementary Fig. S2D). We tested dosing daily and twice weekly. We did not observe significant target inhibition in the KPC-46-1 model when dosing twice weekly but observed significant target inhibition when dosing daily (Supplementary Fig. S2B). However, we observed tolerability issues in some mice in the daily dosing group. Therefore, we chose to dose every 48 hours in the KPC-46-1 model, which was well-tolerated, and western blots of peripheral blood mononuclear cell confirmed target inhibition at this dosing level (Supplementary Fig. S2D). TAK-981 significantly improved survival as monotherapy when tumors were established in immunocompetent mice [Fig. 2B (left)], but not in Rag1^{-/-} mice [Fig. 2B (right)]. Rag1 (recombination activating gene 1) is required for variable-diversity-joining rearrangement [V(D)J] recombination to encode immunoglobulin and T-cell receptor molecules. As such Rag1^{-/-} mice contain fully functional innate immune cells, including NK cells, but do not contain mature T and B cells. Because B cells represent approximately 5% of all cells in the tumor (Fig. 2C), these data suggest that the survival benefit seen in immunocompetent mice is mainly mediated by T cells. This contrasted with our prior expectation that SUMOylation drives oncogenesis and cell cycle progression by tumor cell-intrinsic effects (7–9). Our own data show direct inhibition of proliferation by TAK-981 on this organoid line in cell culture (Supplementary Fig. S2F). IHC staining of tumor tissues showed that TAK-981 also inhibited proliferation and enhanced apoptosis as evidenced by Ki67 and caspase 3 cleavage staining, respectively (Supplementary Fig. S2G). Mice died of metastatic disease progression, which was delayed in treated mice in the immunocompetent model, but TAK-981 did not affect primary tumor size (Supplementary Fig. S2E).

To understand the effect of pharmacological inhibition of SUMOylation *in vivo*, we carried out single-cell RNA-seq analyses

**Figure 2.**

Pharmacological SAE inhibition in a mouse PDAC model, which recapitulates the TME of human PDAC, increased survival in a strictly T cell-dependent manner. **A**, A representative ultrasound image of an orthotopic KPC-46-1 tumor in mice. **B**, Kaplan-Meier survival curves show the survival difference between control mice and TAK-981-treated mice injected orthotopically with KPC-46-1 cells in WT (left) and Rag1^{-/-} mice (right), dosed with 15 mg/kg every 48 hours. **C**, (Left) UMAP visualization plot of PCA on all cells from KPC-46-1 tumors. Tumors were harvested from both vehicle control- and TAK-981-treated mice when established in WT mice. The clusters are separated into specific cell types: B cells, DC, myeloid, granulocytes, T/NK cells, CAF, ductal cells, and endothelial cells. (Right) Dot plot of representative marker genes for each cluster/cell type. The dot size represents the percentage of cells in the cluster that express the corresponding gene. The color scale of red to yellow represents the average expression level of the gene in the cluster. **D**, (Left) UMAP visualization plot of PCA on ductal cell types from KPC-46-1 tumors. Tumors were harvested from both vehicle control- and TAK-981-treated mice when established in WT mice. (Right) Dot plot of representative marker genes for each cluster/cell subtype. The dot size represents the percentage of cells in the cluster that express the corresponding gene. The color scale of red to yellow represents the average expression level of the gene in the cluster. **E**, Dot plot showing the effect of TAK-981 on the expression of genes in the two ductal cancer cell clusters. The dot size represents the percentage of cells in the cluster that express the corresponding gene. The color scale of red to yellow represents the average expression level of the gene in the cluster. **F**, Cell population proportion test comparing the proportions of ductal cell populations in vehicle control- and TAK-981-treated samples using scProportionTest (22). Positive Log₂FC values indicate the population of the corresponding cell subtype is larger in proportion in the TAK-981 treated group. The negative values indicate that the proportion of the corresponding population has decreased upon TAK-981 treatment. The error bars and the fold difference threshold of Log₂FC = 0.58 indicate the statistical significance of those differences. The significant values that are above the threshold and with FDR below 0.05 are shown in red. The confidence interval for the magnitude difference is calculated through bootstrapping. **G**, GSEA analysis of the top activated and inhibited pathways in the two ductal cancer cell clusters. **H**, Dot plot showing the effect of TAK-981 on the expression of MHC class I and class II genes in the two ductal cancer cell clusters. The dot size represents the percentage of cells in the cluster that express the corresponding gene. The color scale of red to yellow represents the average expression level of the gene in the cluster.

of two KPC-46-1 mouse tumors treated for 2 weeks with TAK-981 and two similarly sized tumors from the control group. The immune cell types were identified and classified using highly expressed genes as previously described (Fig. 2C; Supplementary Fig. S1B; Supplementary Table S2; ref. 28). TAMs represented the largest population among immune cells (Fig. 2C). In addition, CAFs, endothelial cells, dendritic cells, granulocytes, and B, T, and NK cells were also identified (Fig. 2C). Thus, this model recapitulates human PDAC tumors in that it is TAM rich, contains all major immune and nonimmune stromal cell types found in human PDAC tumors, and cancer cells occupy less than 50% of total cells of the tumors. We observed a reduction of B cells in the tumors and systemically.

Although TAK-981 did not have a significant effect on tumor growth in the immunocompromised mouse model, cancer cells in the TME are affected by TAK-981 *in vivo*. As an organoid line derived from a KPC model (27), we observed two clusters of ductal cancer cells (Ductal 1 and 2) along with noncancerous Ductal 3 and metaplastic acinar (acinar-to-ductal metaplasia) cells (Fig. 2D). Cancer stem cell markers, such as *Aldh1a1*, had higher expression in Ductal 1 than Ductal 2 cells (Fig. 2E). Ductal 2 cells expressed higher level of *Mki67* and *Top2a* than Ductal 1 cells (Fig. 2E). Violin plots with *P* values are shown in Supplementary Fig. S3A and S3B. TAK-981 exposure did not significantly reduce the ductal cancer cell population, consistent with lack of inhibition of tumor progression in *Rag1^{-/-}* mice, but it increased the population of the noncancerous Ductal 3 cell population (Fig. 2F). TAK-981 treatment did alter gene expression in ductal cancer cells, reducing *Mki67* and *Top2a* in Ductal 2 cells (Fig. 2F) and reducing the expression of cancer stem cell marker *Aldh1a1*, and EMT markers (*Cdh2*, *S100a4*, and *Snai2*) in Ductal 1 cells (Fig. 2E). GSEA using the fgsea method (29) showed that TAK-981 treatment reduced oxidative phosphorylation in both Ductal cancer cell populations and activated apoptosis and the TNF α pathway (Fig. 2G). Cell cycle-related gene sets did not show significant changes, unlike those observed *in vitro* (30).

The expression of major histocompatibility complex class I (MHC-I) is required for antitumor adaptive immunity by presenting neoantigens to T cells. Tumor cells can evade immunity by reducing or losing the expression of MHC-I molecules. PDAC tumor cells often have low expression of MHC-I molecules which allows them to evade antitumor T-cell response (31). Similar to human PDAC tumors, MHC-I molecules were expressed in less than 50% of cells and at low levels in cancer cells in this mouse model (Fig. 2H). SAE inhibition increased both the expression levels and percentage of cells expressing MHC-I genes in both Ductal 1 and Ductal 2 cancer cells (Fig. 2H). Violin plots with *P* values are shown in Supplementary Fig. S3A and S3B.

SAE inhibition significantly shifts TAMs toward antitumor phenotypes.

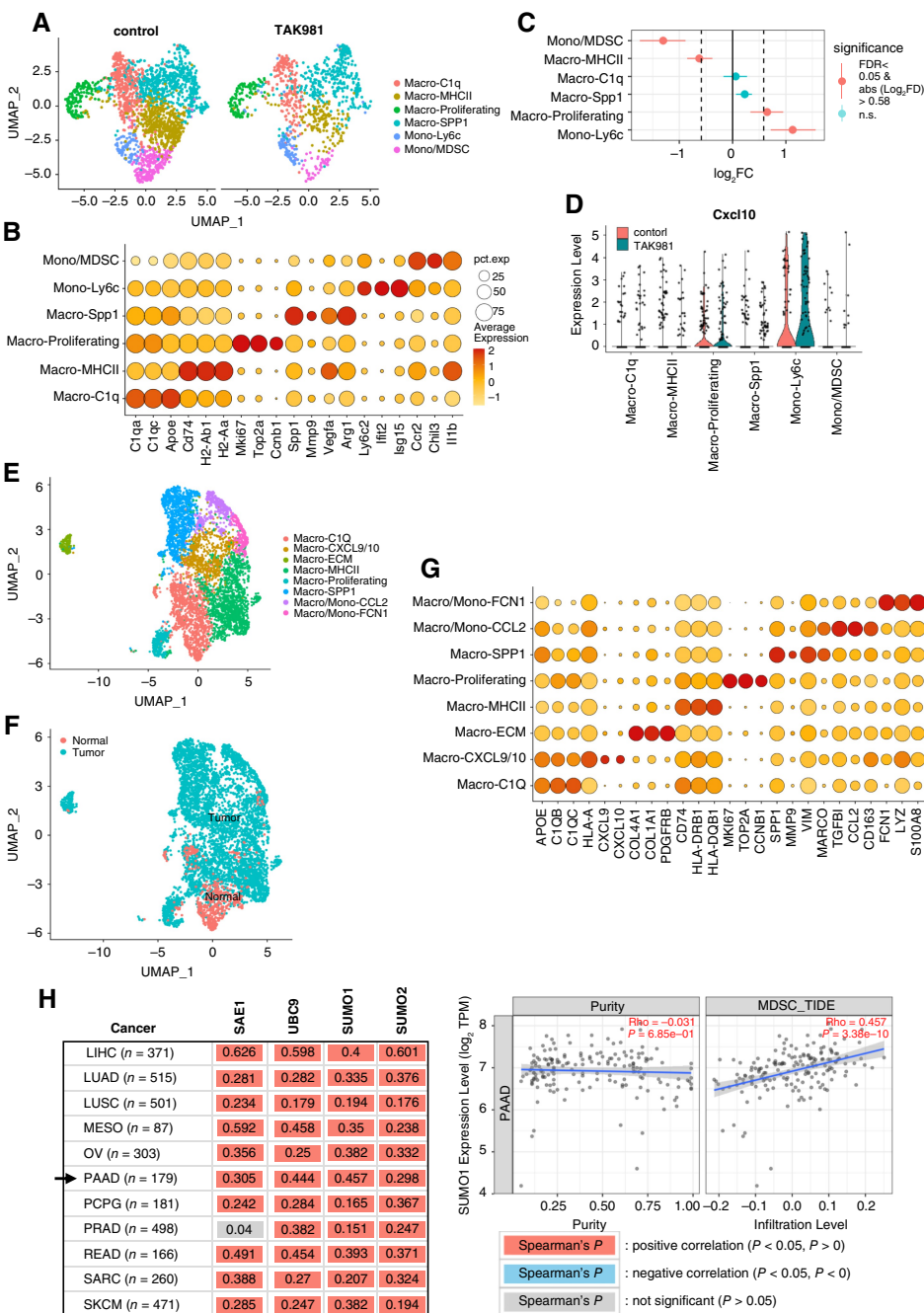
PDAC is rich in TAMs, which are thought to promote immune suppression and T-cell exclusion. We analyzed the effect of pharmacological inhibition of SUMOylation on TAMs. GSEA showed that TAK-981 treatment activated both type I interferon (IFN) and IFN γ targeted gene expression in TAMs (Supplementary Fig. S4A). Single-cell transcriptomics have revealed more subtypes of TAMs than traditionally classified "M1" and "M2" types (11, 32, 33), and, consistent with previous findings, the TAMs consist of six major subtypes (Fig. 3A and B). TAK-981 treatment altered the proportions of the subtypes significantly (Fig. 3C). Consistent with fewer TAM cells in

single-cell transcriptome data, total macrophages in a tumor were reduced by TAK-981 treatment as shown by CD68 IHC (Supplementary Fig. S2G). The Macro-Ly6c subtype increased the most (Fig. 3C) and expressed type I IFN-stimulated genes (i.e., *Ifit2*, *Isg15*; Fig. 3B). This subtype is the main producer of chemokine *Cxcl10* (Fig. 3D), a chemoattractant for T and NK cells, and the expression of *Cxcl10* also increased upon TAK-981 treatment (Fig. 3D). The macroproliferating subtype also expressed *Cxcl10*, and the proportion of this subtype increased upon TAK-981 exposure. Because IFN-I and IFN γ are among the top upregulated pathways in myeloid cells, the most abundant stroma cells, we examined IFN-I and IFN γ stimulated genes by RNA expression analysis (qPCR) of tumor lysates. We confirmed increased expression of IFN γ target genes, such as *Pdl1*, *Il1b*, and *Cxcl9*, but variations in *Ifib1* and *Cxcl10* expression (Supplementary Fig. S4B) between mice were too large to yield statistically significant differences.

Single-cell transcriptomics allowed the identification of corresponding TAM subtypes in human PDAC samples. In human tissues, myeloid cells are more enriched in tumors than noncancerous pancreatic tissues (Fig. 3E and F). The myeloid cells are classified into eight subtypes according to gene expression profiles (Fig. 3E–G). The Macro-Ly6c subtype in mice can be mapped to the Macro-CXCL9/10 in human samples, which only exists in cancer tissues and expresses higher levels of these chemokines than other subtypes. The macroproliferating subtype can also be mapped to human samples and predominately exists in tumors. These findings suggest that SAE inhibition may similarly increase these subtypes in human PDAC and increase their expression of CXCL9/10 chemokines. Indeed, TAK-981 monotherapy increased CXCL10 in patients' blood in Phase I clinical trials (14).

The MDSC, which confers immunosuppressive functions (36), was the cell type reduced the most upon pharmacological inhibition of SUMOylation by TAK-981 (Fig. 3C). Macro-CCl2 and Macro-FCN1 are specific to cancer tissues in human samples and have high MDSC gene expression signatures as identified previously (37) and marked by expression of M2-like genes, such as *TGFB1* (Fig. 3G). These subtypes likely correspond to the MDSC population in mouse PDAC tumors. Analysis of immune infiltrates provided by the TIMER2.0 webserver (35) identified positive correlations between MDSC populations and the expression of SUMOylation-related genes. Higher expression of SUMOylation-related genes correlates with increased MDSC populations across many human tumor types, including PDAC (Fig. 3I). As an example, SUMO1 expression positively correlates with MDSC levels in PDAC samples [*P* < 0.0001; Fig. 3I (right)]. These findings suggest that pharmacological inhibition of SUMOylation is a potential strategy to reduce the immunosuppressive MDSC population in PDAC tumors.

Besides MDSC, SAE inhibition by TAK-981 suppressed the expression of genes known to promote tumor progression. SUMOylation inhibition reduced the proportions of the Macro-MHC-II subtype in our mouse model—this subtype can be mapped to a tumor-dominating subclass of macrophage Macro-MHC-II in human samples (Fig. 3A and E) that expresses angiogenesis-promoting VEGFA and the proinflammatory cytokine IL1B (Fig. 3B). SAE inhibition reduced the proportions of this subtype in our mouse model (Fig. 3C). Although TAK-981 reduced populations of TAM subtypes that express tumor-promoting and immune suppression factors, TAK-981 treatment increased the total TAM expression of genes traditionally associated with the antitumor M1-like phenotype (including *Cd86*, *Nos2*, *Ccl2*, *Ccl3*, *Ccl4*, *Cxcl9*, and *Cxcl10*) and enhanced genes related to IFN and TNF response such as *Cd40*, *Irf3* and *Irf5*, *Il18*, *Trl4*, and

**Figure 3.**

TAK-981 induces changes in TAM to reduce the expression of immune suppressive genes and subtypes, but increase the subtypes and genes that support T-cell recruitment. **A**, UMAP visualization plot of TAM in the mouse model. Different subtypes of macrophages were identified as previously described (32–34). **B**, Dot plot of representative marker genes for each macrophage/monocytic cell subtype. **C**, Cell population proportion test comparing the proportions of myeloid populations in vehicle control- and TAK-981-treated samples using scProportionTest (22). Positive Log₂FC values indicate the population of the corresponding cell subtype is larger in proportion in the TAK-981-treated group. The negative values indicate that the proportion of the corresponding population has decreased upon TAK-981 treatment. The error bars and the fold difference threshold of Log₂FC = 0.58 indicate the statistical significance of those differences. The significant values that are above the threshold and with FDR below 0.05 are shown in red. The confidence interval for the magnitude difference is calculated through bootstrapping. **D**, Violin plot of Cxcl10. It was mainly expressed in the Mono-Ly6c subtype and the expression increased upon TAK-981 treatment. **E**, UMAP visualization plot of myeloid cells in human PDAC and noncancerous pancreas dataset. The cells are categorized into specific subtypes. **F**, UMAP visualization plot of the same cells, but the cells are indicated as “normal” or “tumor” based on the origins of the cells. **G**, Dot plot of representative marker genes for different myeloid cell subtypes. **H**, The associations between MDSC in the TME and SUMOylation-related genes in The Cancer Genome Atlas using TIMER2.0 (35). Significant positive associations (red color) were observed for PDAC (PAAD) and other multiple cancer types. Correlation of MDSC tumor infiltration with the expression of the SUMO1 gene is shown on the right.

Stat1 (Supplementary Fig. S4C). In addition, the expression levels of genes traditionally associated with the M2-like phenotype were reduced, such as *Mrc1*, *Arg1*, *Stat3*, *Il10ra*, and *Vegfa*, *Il6*, and *Tgfb* (Supplementary Fig. S4C). To test the statistical significance of these changes, we analyzed these genes collectively using the M1 score (defined by the expression of *Cd86*, *Nos2*, *Stat1*, *Cxcl9*, and *Cxcl10*) and M2 score (defined by the expression of *Cd163*, *Arg1*, *Mrc1*, *Stat3*, *Msr1*, and *Vegfa*) and found this difference to be significant (Supplementary Fig. S4D). Together, these data suggest that SAE inhibition results in shifts in TAM subtypes as well as changes in gene expression within subtypes that reduce immunosuppression within the TME.

SAE inhibition reduced CAF cell interactions.

PSCs and CAFs in the TME interact with cancer cells and immune cells to promote tumor progression and immune suppression (38–41). In the human PDAC TME, CAFs and PSCs have distinct gene expression profiles from fibroblasts found in noncancerous tissues (Fig. 4A and B; Supplementary Fig. S5A). The majority of CAFs belong to the previously identified myofibroblastic CAF (myCAF) category (43). In addition, inflammatory CAFs (iCAF) are also tumor-specific. The software CellChat (44) was used to analyze CAF interaction with other cells in the TME. Cell-cell interaction strength is calculated from receptor/ligand expression and the

extent of gene expression changes reflective of the signaling pathways triggered by the cell-cell interactions (44). A circle plot illustrates the cell-cell interactions in human PDAC tumors, in which the cell-cell interaction strengths are represented by the thickness of the lines (Fig. 4C). Indeed, cell-cell interactions indicate that CAFs and PSCs exhibit the strongest interactions with ductal cancer cells (Fig. 4C).

In the PDAC mouse model, similar CAF subtypes were identified (Fig. 4D; Supplementary Fig. S5B). iCAF and myCAF correspond to those in the human PDAC according to gene expression profiles. PSCs were also identified in the mouse model (Fig. 4D). apCAF form a distinct cluster in the mouse model but are distributed into iCAF and myCAF in human PDAC samples (43). Pharmacological inhibition of SUMOylation did not change the total PSC and CAF subtype proportions in the mouse model significantly (Fig. 4E) but altered their gene expression. GSEA revealed significant increases in IFNa and IFN γ target genes and a significant reduction of oxidative phosphorylation (Fig. 4F).

SAE inhibition significantly reduced CAF-mediated cell-cell interaction strengths with nearly all cell types. Similar to the human PDAC TME, CAFs in the mouse model also exhibit strong interactions with cancer cells and other cells in the TME, as shown by the thickest lines (Fig. 4G). SAE inhibition caused the strongest reduction of CAF interactions with other cell types but induced the strongest increase in T/NK cell interactions with other cell types (Fig. 4H; PSCs and CAFs in mouse samples were grouped together in this analysis). This is consistent with the significantly altered gene expression seen in CAFs (Fig. 4F). Along with the previous findings that CAFs in the TME promote tumor progression (38–41), these findings suggest that SAE inhibition may reduce the tumor-promoting functions of CAFs.

TAK-981 alters T-cell phenotypes and increases T-cell infiltration into the TME

The PDAC TME is often characterized by poor penetration of cytotoxic T cells. Indeed, in the control group, CD4 and CD8 T cells were mostly restricted to the peri-tumoral areas [Fig. 5A (top)]. Following treatment with TAK-981, however, T cells became widely distributed throughout the tumor tissues, and peri-tumoral T cells were visibly reduced [Fig. 5B (bottom)]. Therefore, pharmacological inhibition of SUMOylation increased T-cell infiltration into the TME.

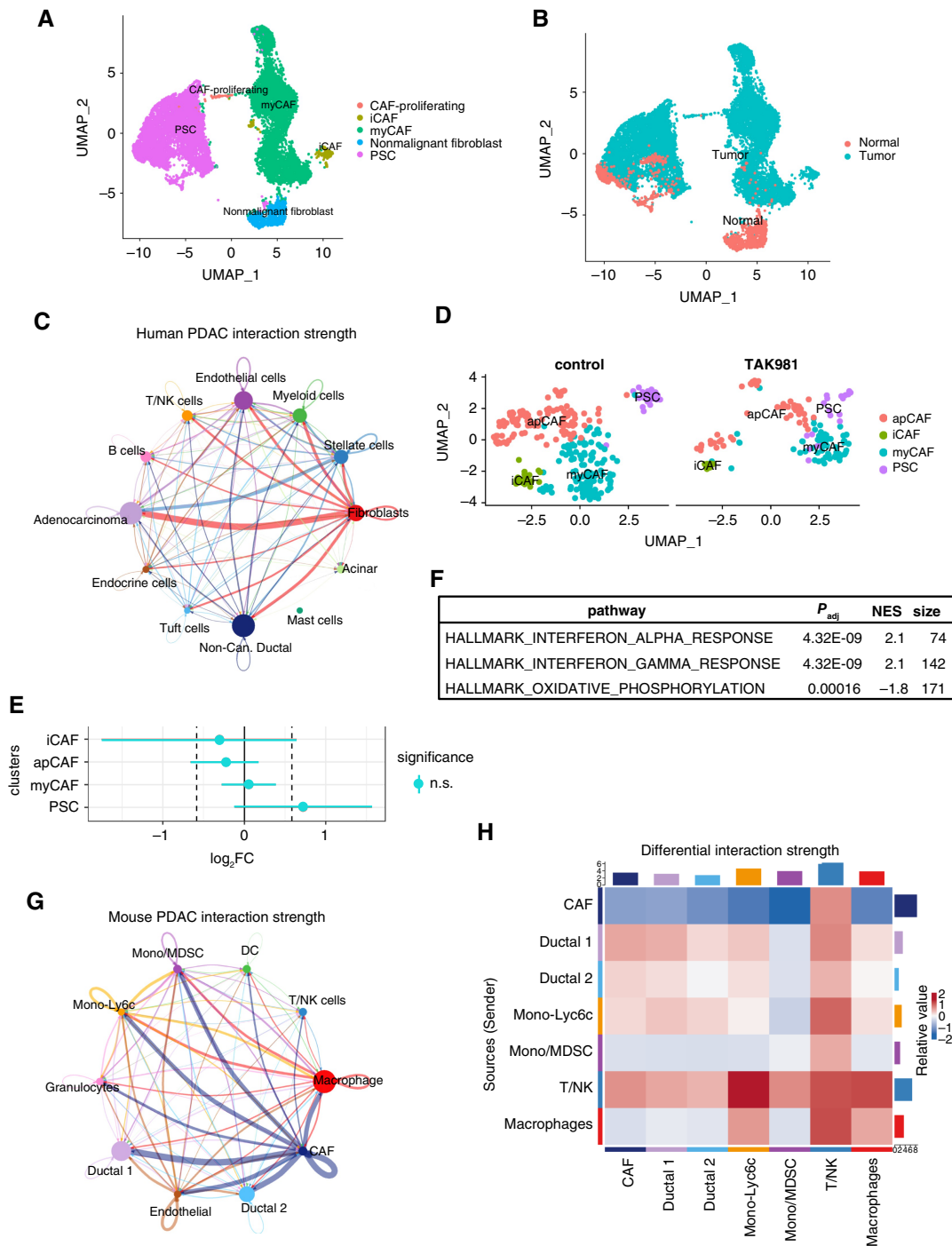
The mouse tumor-infiltrating T and NK cell types were also analyzed using single-cell transcriptomics for the effect of pharmacological inhibition of SUMOylation (Fig. 5B and C; Supplementary Fig. S6). We observed a dramatic reduction of regulatory T cells (Treg) with TAK-981 treatment (indicated in pink; Fig. 5B–D). This is consistent with the analysis of multiplex IF imaging showing a ~20-fold reduction in the frequency of Tregs (CD4 $^+$ -FoxP3 $^+$) from 17 cells/mm 2 in the control group to 0.8 cells/mm 2 in the TAK-981 treatment group (Fig. 5A and E). We also observed changes in other T-cell subtypes. Control tumors contained a much larger number of naïve-like T cells than TAK-981 treated tumors (Fig. 5B and C). In addition, a subgroup of effector-like T cells in TAK-981-treated tumors, indicated as Teff1, was increased as compared with control tumors, whereas another subgroup of effector-like T cells, indicated as Teff2, had the opposite changes. Teff1 cells express the highest level of Nkg7 among all cell types examined. Nkg7 has been associated with antitumor cytotoxicity and accumulation of T cells in the TME and immune checkpoint

inhibition therapy efficacy (45). Furthermore, we observed CD4-expressing effector memory-like cells in TAK-981-treated tumors only and not in control tumors (Fig. 5B–D).

TAK-981 increased the expression of activation markers and costimulatory receptors but reduced the expression of some exhaustion markers. The activation markers and costimulatory molecules that were increased include *Cd28*, *Ifng*, *Cd69*, *Cd44*, *Tnfrsf4* (OX-40), *Tnfrsf9* (4-1BB), and *Gzmb* (Fig. 5F). The expression of *Pdcld* (PD1) and *Ctla4* was detected in more cells upon TAK-981 exposure. However, the expressions of *Havcr3* (Hepatitis A virus cellular receptor 2, *Tim3*), *Tigit*, and *Lag3* were detected in less than 20% of these cells (Fig. 5F). To further investigate the expression of these low expression exhaustion markers, we performed IF staining for Tim3 (Fig. 5A and E). Immunofluorescence staining showed that there was an overall reduction in cell staining for Tim3 (Fig. 5E). The NK cell proportion did not change substantially. Taken together, pharmacological inhibition of SUMOylation not only resulted in increased T-cell infiltration into the TME but also altered T-cell subtype proportions in the TME by reducing naïve T cells and immunosuppressive Tregs and increasing effector and memory T cells and their activation while suppressing some T-cell exhaustion markers.

To evaluate TAK-981 *in vivo* in a different orthotopic model, a 2D KPC4580P cell line (21) was implanted into the tail of the pancreas of immunocompetent mice to establish tumors. Tumor growth was monitored by high-resolution ultrasound. Once tumors reached 5 to 7 mm in diameter, mice were randomized to one of the treatment groups: TAK-981 (7.5 mg/kg) versus vehicle control that was delivered via injection twice weekly for four doses as previously described for this inhibitor other tumor models (12). Tumor growth in the TAK-981 group was reduced compared with control, and this effect persisted to day 20, even though treatment with TAK-981 was stopped on day 11 (Fig. 6A). Flow cytometry was performed on tumors, revealing increases in IFN γ $^+$ CD8 $^+$ T cells, NK cells, and CD4 $^+$ T cells, reduction of PD1 $^+$ CD8 $^+$ T cells, although statistical significance ($P < 0.05$) was not achieved. We observed a reduction of CD68, a general macrophage marker, by IHC (Supplementary Fig. S2G) with SUMOylation inhibition. However, no change in the M1:M2 ratio was observed in CD45 $^+$ CD11b $^+$ F4/80 $^+$ cells in which CD206 lo MHC-II hi cells were classified as M1 macrophages and CD206 hi MHC-II lo cells were classified as M2 macrophages (Fig. 6B). These data are consistent with the KPC46-1 model in that TAK-981 treatment-induced increases in cytotoxic lymphocytes, increased T-cell activation and reduced exhaustion.

Analysis of human PDAC datasets suggests a direct role of SUMOylation in regulating T-cell activation, differentiation, and Treg maintenance. In human samples, T and NK cells are rare in noncancerous pancreas tissues (Fig. 7A–C), suggesting the immune privilege of noncancerous pancreas. For T cells, various CD8 $^+$ and CD4 $^+$ subtypes were identified, including naïve, central memory, effector memory, exhaustive, and Treg using the highly expressed genes (Fig. 7C). Supporting our findings in the mouse model, effector and memory-like T cells have lower expression of SUMOylation-related genes compared with Treg and exhausted T cells (Fig. 7D), suggesting the lower dependency of effector and memory-like T cells on SUMOylation than Treg and exhausted T cells. Analysis of tissue microarray panels of 15 human noncancerous pancreas tissues and 76 PDAC tissues (Supplementary Fig. S7) confirmed that T cells are not abundant in PDAC tissues, but there are even fewer CD8 $^+$ T cells in noncancerous pancreas tissues than PDAC tissues.

**Figure 4.**

SAE inhibition remodeled CAF/PSC and inhibited their interactions with tumor cells and other cell types in the TME. **A**, UMAP visualization plot of PSC and CAF in human PDAC/pancreas data. Cells are classified into subtypes. **B**, UMAP visualization plot of PSC and CAF in human PDAC/pancreas data. Cells are grouped into either “normal” or “tumor” based on the cells’ origins. **C**, Circle plot of cell-cell interaction strengths in human PDAC samples. The interaction strengths are shown by the thickness of the lines with thicker lines representing stronger interactions. **D**, UMAP visualization plot of PSC and CAFs in mouse KPC-461 data. Cells are classified into specific subtypes. **E**, Proportion test plot of mouse PSC/CAF populations, showing no significant increase or decrease in the populations of the various cell subtypes. **F**, GSEA shows the most upregulated and downregulated pathways in CAFs upon TAK-981 exposure. **G**, Circle plot of cell-cell interaction strengths in human PDAC samples. The interaction strengths are shown by the thickness of the lines. **H**, Comparative plots of incoming and outgoing interaction strengths comparing TAK-981-treated tumors with controls. Interaction strengths were calculated via CellChat (42). Blue or red indicates reduced or enhanced cell-cell interactions, respectively, in TAK-981-treated samples compared with the control. Darker red or blue colors indicate more increased or decreased interaction strengths, respectively.

To further analyze the relationship between the SUMOylation pathway and T-cell activation and exhaustion, we created a SUMO gene expression score that consists of the expression of SUMO1, SUMO2, SUMO3, UBA2, and UBE2I using Seurat (24). Similarly, we created a CD8 T-cell activation score that consists of CD69 and CD44, and a CD8 T-cell exhaustion score defined by the expression of PDCD1, CTLA4, TIGIT, FIBP, TNFSF10, HAVCR2, and LAG3. There was a significant inverse correlation between the SUMO score and T-cell activation score [Fig. 7E (left)] and a significant positive correlation between SUMO score and exhaustion score [Fig. 7E (right)]. The analyses from these human datasets support the finding that pharmacological inhibition of SUMOylation in our mouse model reduces Tregs and enhances T-cell activation, memory formation, and effector function (Fig. 5). The multiple effects of TAK-981 treatment on T cells are likely important for the development of adaptive immunity as shown by the loss of survival benefit in *Rag1^{-/-}* mice, in contrast to that observed in WT mice (Fig. 2B).

Discussion

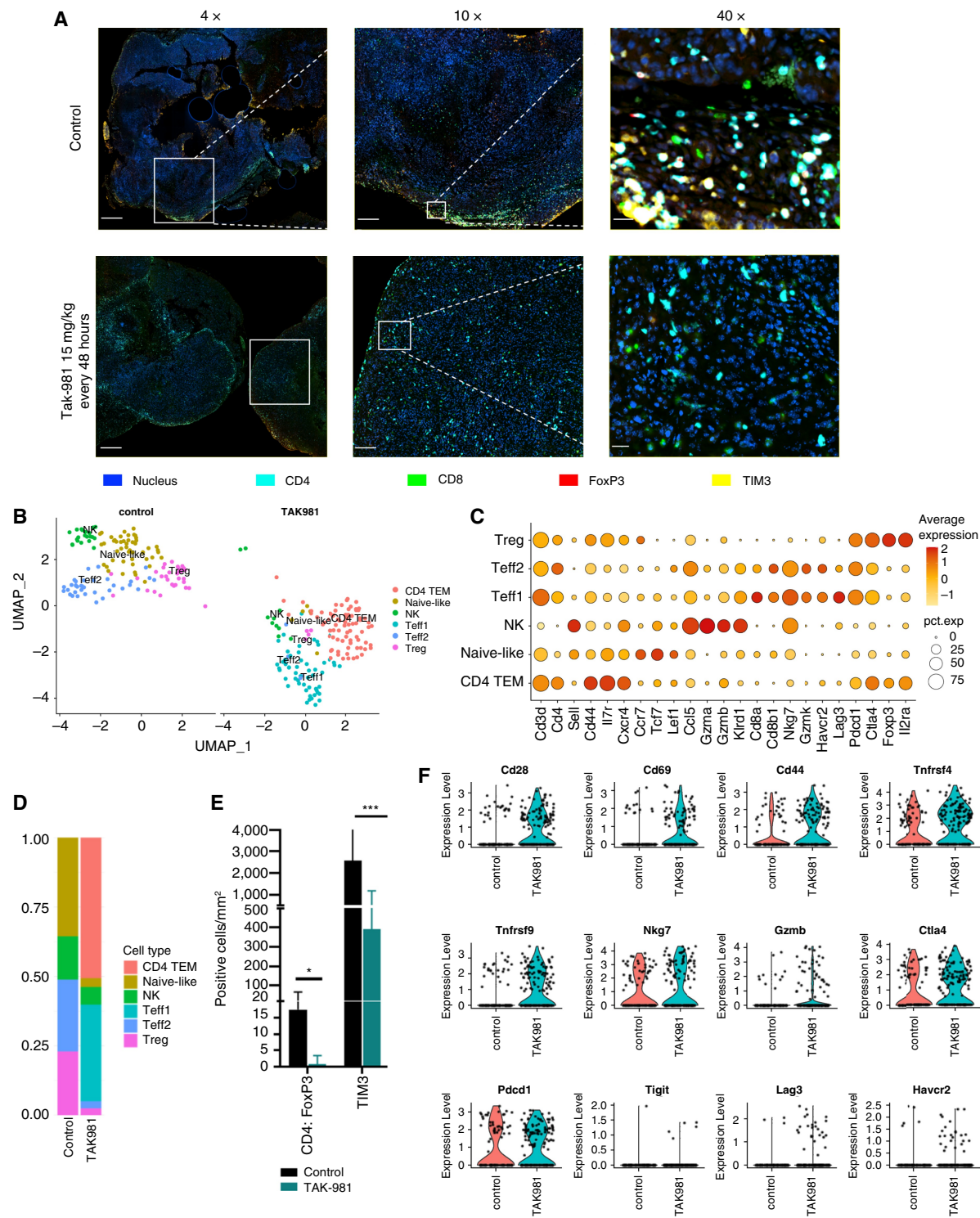
Most studies of SUMOylation in cancers have focused on epithelial cancer cell biology. However, cancer cells are often outnumbered by stromal cells in TME (Fig. 1), and the cell–cell interactions in the TME, through direct ligand–receptor interactions and through secreted cytokines and other factors, strongly affect cancer progression and response to therapies (11). The SUMOylation pathway is active in cancer cells as well as immune and nonimmune stromal cells, and thus, it is important to understand the impact of SAE inhibition in the context of relevant TME. In this study, SAE inhibition produced therapeutic benefits in two different orthotopic syngeneic mouse models derived from the KPC genetic model (27). Although some effects were seen on tissue markers of cellular proliferation and apoptosis, the main effect of SAE inhibition was the induction of antitumor adaptive immunity (Figs. 2 and 6). Transcriptomic analysis at single-cell resolution allowed us to examine the effects of SAE inhibition on each cell type in the context of a relevant TME. *In vivo*, tumor cell transcriptome analysis showed that SAE inhibition did not alter Myc, KRas, and cell cycle pathways as expected from previous studies of cancer cells in the absence of TME (7–9) but altered pathways that are less well described in association with SUMOylation, including reduced oxidative phosphorylation and enhanced TNF α signaling. This could be because of TME effects and/or an *in vitro/in vivo* difference in the magnitude or duration of SUMO inhibition by TAK-981. Single-cell transcriptomics allowed the mapping of mouse cells to the corresponding cell types/subtypes in human tumors to provide insights for the successful translation of the findings to improve treatment responses in PDAC.

Gene expression changes in cancer cells by TAK-981 monotherapy likely played a critical role in developing antitumor immunity. One of the key mechanisms for PDAC and many other cancer cells to evade immune surveillance is the downregulation of MHC-I that is required for the presentation of neoantigens to cytotoxic T cells (31). Similar to that observed in human PDAC tumors, MHC-I molecules are expressed in 20% to 40% of cancer cells at low levels in our mouse model (Fig. 2H). SAE inhibition induced MHC-I expression in up to 80% of cancer cells and markedly increased the expression levels (Fig. 2H). MHC-I gene upregulation in PDAC cells would enhance neoantigen presentation to cytotoxic T cells and thus likely contribute

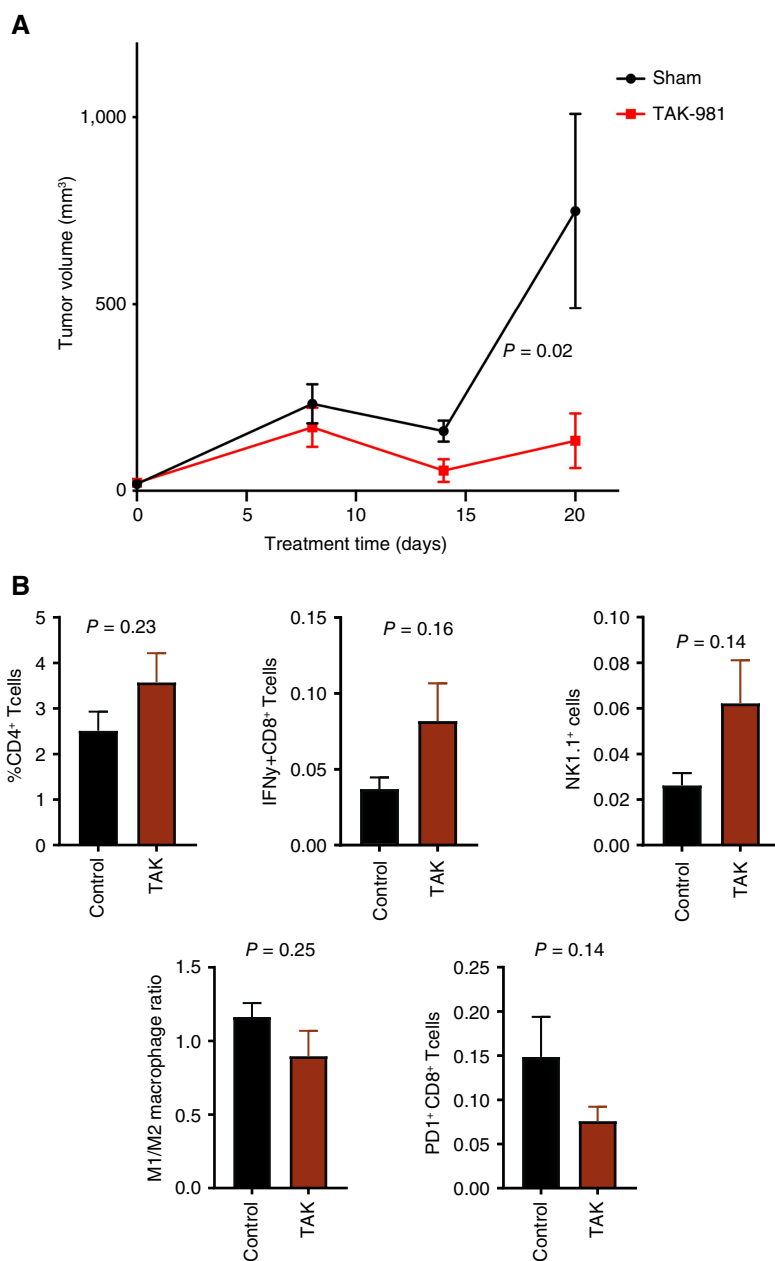
to antitumor T-cell response induced by TAK-981. The mechanism for such upregulation and its role in antitumor immunity requires further investigations. Thus, pharmacological inhibition of SUMOylation is a potential strategy to enhance MHC-I expression of cancer cells to induce antitumor immunity.

Changes in TAM and CAFs in the TME by TAK-981 monotherapy likely contributed to the antitumor T-cell response. Single-cell transcriptome analyses indicate that CAF/PSCs in untreated human and mouse PDAC tumors exert strong cell–cell interactions with ductal cancer cells (Fig. 4). This is in line with the previous finding that tumor cells and CAFs engage in reciprocal signaling to amplify oncogenic signaling in PDAC (46). SAE inhibition significantly reduced CAF/PSC interactions with cancer cells and other cell types (Fig. 4J), suggesting that CAFs are reprogramed by SAE inhibition to reduce their tumor-promoting effects. SAE inhibition reduced MDSCs in the mouse TME. Direct regulation of MDSCs by SUMOylation is suggested by a positive correlation of MDSC levels with the expression of SUMOylation-related genes in human PDAC and other tumor types (Fig. 3I and J). SAE inhibition reduced TAM numbers in a dose frequency-dependent manner (Supplementary Fig. S2G), whereas it increased the proportion of Ly6c-expressing monocytes that have type I IFN signatures. The Ly6c-high monocytes with type I IFN signatures were shown to be bone marrow-derived and have phagocytic functions (47), and their increase in TME likely reflects increased infiltration in response to SAE inhibition. This subtype shows the highest expression level for *Cxcl10*, and their *Cxcl10* expression further increased upon TAK-981 treatment (Fig. 3D). Although *Cxcl9* was not well-detected in the single-cell dataset, qPCR of tumor lysates showed an increase of *Cxcl9* by TAK-981 treatment. Upregulation of *Cxcl9* and *Cxcl10* is consistent with previous findings that SUMOylation inhibition activates IFN β and the expression of IFN γ target genes (48). The increase in *Cxcl9* and *Cxcl10* chemokine expression, which are chemo attractants for T cells, is consistent with increased T/NK cell infiltration into the TME upon SAE inhibition in both KPC-46-1 and KPC4580P orthotopic models (Figs. 5A and 6). Thus, pharmacological inhibition of SUMOylation is a potential strategy to remodel CAFs and TAM in the TME to reduce their tumor-promoting and immune-suppressive functions.

Our data suggest that SUMOylation regulates T-cell activation and differentiation. Large populations of naïve T cells were observed in the PDAC TME in our mouse model and in human tumors in our analysis (Figs. 5B and 7A) and previously (23, 49). SAE inhibition diminished naïve T-cell numbers and increased CD4 $^{+}$ memory T cells in the TME (Fig. 5B). The important role of CD4 $^{+}$ T cells in antitumor immune response in PDAC was previously shown (50). SAE inhibition also increased T-cell activation-related genes (Fig. 5F) and reduced the terminal exhaustion marker Tim3 (Fig. 5E) in the orthotopic KPC-46-1 model. Analysis of human PDAC samples reveals higher expression of SUMOylation-related genes in exhausted T cells and Tregs than effector and memory T cells, suggesting a stronger dependence of exhausted T cells and Tregs on SUMOylation than effector and memory T cells. Indeed, previous studies have shown that SUMO2 is required for Foxp3 expression, and exposure of primary human tissues with TAK-981 reduced the viability of Tregs (51, 52). In addition, SAE inhibition could inhibit T-cell exhaustion indirectly by modulating the TME, such as inhibition of Tgf β expression in myeloid cells (Supplementary Fig. S4B). Furthermore, transcription factors, such as AP1 and NFAT involved in the expression of activation and

**Figure 5.**

Pharmacological inhibition of SUMOylation increased T-cell expression of activation markers and costimulatory receptors, inhibited some exhaustion markers, and promoted the formation of memory phenotypes. **A**, Multiplex IF imaging to detect CD4, CD8, FoxP3, and Tim3. Bars in the 4× images represent 1 mm. The bar in the 10× image in the control tumor represents 200 μm and in the TAK-981 treatment tumor represents 250 μm. Bars in the 40× images represent 20 μm. **B**, Split UMAP visualization of T/NK cells comparing control and TAK-981-treated tumors. **C**, Dot plot of representative marker genes for different T/NK cell types. **D**, Percentage of different cell subtypes in control and TAK-981 treated tumors. **E**, Quantification of the IF image of **A** using the software QuPath. **F**, Violin plots of T-cell activation and exhaustion marker gene expressions within CD3+ cells.

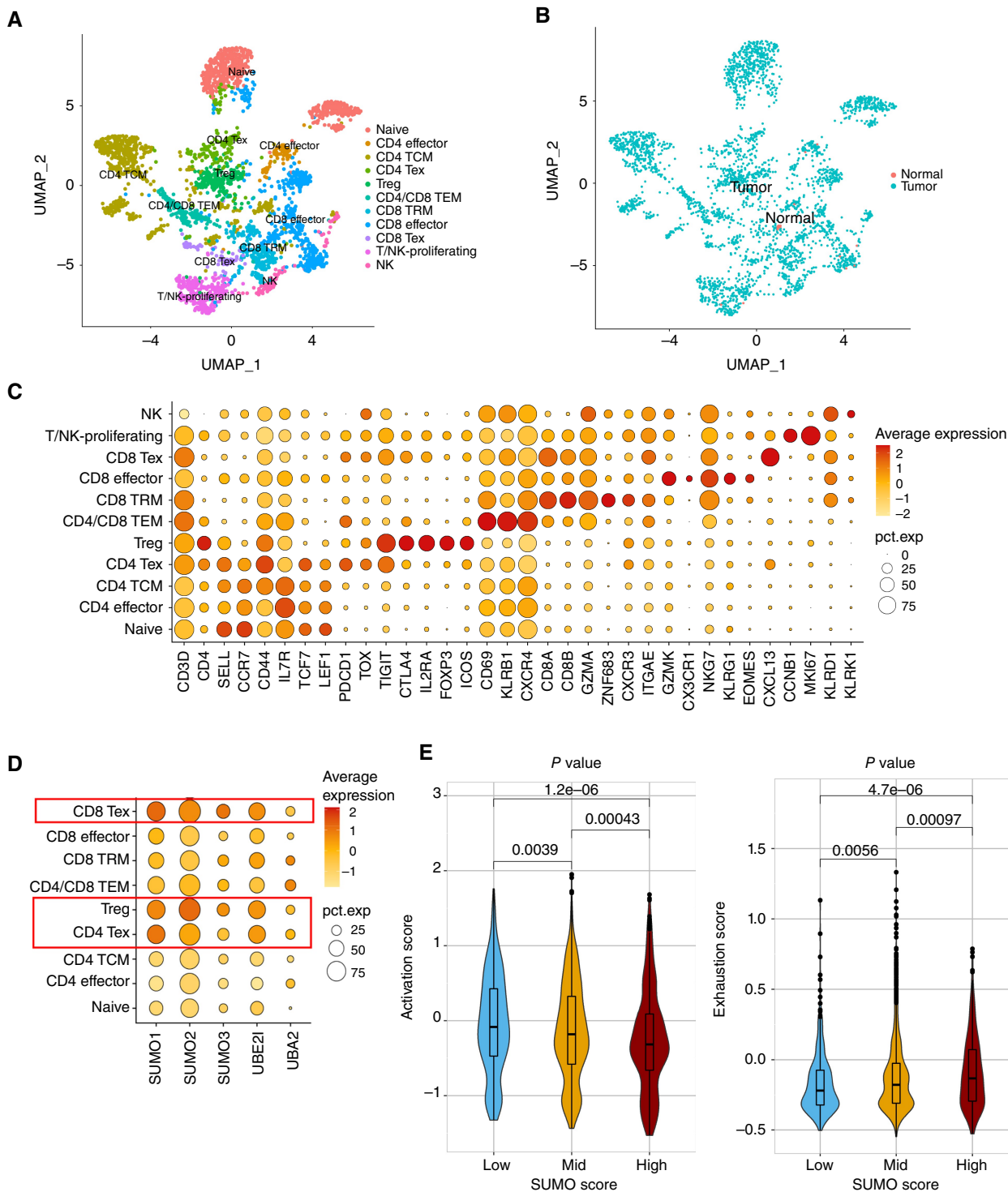
**Figure 6.**

Treatment of orthotopic KPC458OP model with TAK-981. **A**, Mean tumor volumes in TAK-981 treated group and the control group. Analysis of the growth was performed by paired *t* test. **B**, Flow cytometry of tumors harvested at day 14. Although the differences are not statistically significant, the trend is apparent. Statistical comparison was performed by unpaired *t* test.

Downloaded from http://aacjournals.org/mct/article-pdf/23(11)/1597/351983/mct-23-0572.pdf by NYU Medical Center user on 20 November 2024

costimulatory receptors and cytokines, are regulated by SUMOylation (53–55). Future studies are needed to further understand the role of SUMOylation in T-cell activation and differentiation. Changes in cancer cells and immune and nonimmune stromal cells in the TME by SUMOylation inhibition have significant implications for designing future combination therapy. SAE inhibition could synergize with adaptive T-cell therapy, such as tumor-infiltrating lymphocyte therapy, by enhancing T-cell infiltration and promoting activation and memory phenotype formation, enhancing neoantigen presentation on cancer cells, and removing immune suppression of TAM and CAF.

Similarly, these properties can enhance cancer vaccine therapy not only by enhancing dendritic cell activation and T-cell priming through type I IFN response (12), but also by enhancing antitumor T-cell responses through mechanisms uncovered here. We did not observe synergy of TAK-981 with a PDL1-blocking antibody (Supplementary Fig. S8). However, SAE inhibition may synergize with other immune therapies that enhance antigen presentation/T-cell priming. We observed enhanced TNF pathway activity in multiple cell types. Besides in tumor cells, an increased expression of TNF receptor family members OX-40 and 4-1BB were observed in T cells that provide co-stimulation to

**Figure 7.**

Analysis of T and NK cells in the human PDAC samples shows a direct correlation between SUMOylation-related genes and T-cell activation, exhaustion, and memory formation. **A**, UMAP visualization plot of T and NK cells in human PDAC and noncancerous pancreas dataset. The cells are categorized into specific subtypes. **B**, UMAP visualization plot of the same T/NK cells, but the cells are indicated as "normal" or "tumor" based on the origins of the cells. **C**, Dot plot of representative marker genes for different T/NK cell subtypes. **D**, Dot plot of SUMOylation-related gene expressions in different types of T cells. **E**, Violin plots of T-cell activation scores and T-cell exhaustion scores across different SUMO scores. The activation score was calculated based on the expressions of CD69 and CD44. The exhaustion score was calculated based on the expressions of PDCD1, CTLA4, TIGIT, F1BP, TNFSF10, HAVCR2, and LAG3.

enhance T-cell receptor signaling. TAK-981 treatment also increased TNF receptor family member CD40 on myeloid cells (Supplementary Fig. S4B). The enhancement of CD40 provides a mechanistic rationale for combination therapy with CD40 agonists to enhance antigen presentation. In addition, we observed increased expression of Pvr on tumor cells and dendritic cells, and an increase of CD226 on T cells in the single-cell transcriptomic dataset. Because TIGIT on cytotoxic T cells inhibits interactions between CD226 and Pvr during antigen presentation/T-cell priming and T cell-mediated tumor cell killing, this result suggests that SAE inhibition may synergize with TIGIT-blocking therapy to enhance antigen presentation and T cell-mediated tumor control.

These studies, using a highly specific, clinical-stage SAE inhibitor, allow for rapid bench-to-bedside translation and potential clinical impact. Although we recognize that small molecule inhibitors have potential off-target effects, it is worth noting that TAK-981 is highly specific as shown by the high selectivity over homologous enzymes, and by the target-catalyzed formation of drug-SUMO conjugate as the actual inhibitor, where a SUMO protein is the critical contributor to inhibitory binding of SAE (13).

In summary, our study has demonstrated that a major effect of SAE inhibition in preclinical models of PDAC is the induction of adaptive antitumor immunity. Adaptive immunity through the formation of memory T cells is critical for durable responses to therapy and cures. T cells and other immune and nonimmune stroma cells analyzed in this study commonly exist in other tumor types. Our findings form the basis for future studies targeting SUMOylation to develop an efficacious immune therapy regimen for PDAC and potentially other tumors.

Authors' Disclosures

A.M. Lowy reports grants from Takeda during the conduct of the study. R.R. White reports grants from NIH during the conduct of the study. Y. Chen reports grants from NIH and nonfinancial support and other support from Takeda Pharmaceuticals during the conduct of the study, as well as equity ownership of

Suvalent Therapeutics outside the submitted work. No disclosures were reported by the other authors.

Authors' Contributions

S. Erdem: Data curation, formal analysis, investigation, writing—original draft.
H.J. Lee: Data curation, formal analysis, investigation, visualization, methodology, writing—original draft.
J.S.N. Shankara Narayanan: Data curation, investigation, methodology, writing—original draft, writing—review and editing.
M.D.N. Tharuka: Data curation, investigation, visualization, methodology, writing—original draft.
J. De la Torre: Investigation, visualization.
T. Ren: Investigation, visualization.
Y. Kuang: Investigation, visualization.
T. Abeywardana: Investigation, visualization.
K. Li: Data curation, investigation, visualization.
A.J. Berger: Resources, writing—review and editing.
A.M. Lowy: Resources, supervision, writing—review and editing.
R.R. White: Conceptualization, formal analysis, supervision, investigation, writing—review and editing.
Y. Chen: Conceptualization, formal analysis, supervision, funding acquisition, investigation, methodology, writing—original draft, writing—review and editing.

Acknowledgments

This publication includes data generated at the UC San Diego IGM Genomics Center utilizing an Illumina NovaSeq 6000 that was purchased with funding from a National Institutes of Health SIG grant (#S10 OD026929). We also thank the Biorepository and Tissue Technology Core facility at Moores Cancer Center for IHC and IF staining and Oxana De La Rosa for help. The study described here was supported by grants from NIH (R01CA265410, R01CA212119, R01CA216987, and R01CA155620) and a grant from the Pancreatic Cancer Action Network (19-65). The content is solely the responsibility of the authors and does not necessarily represent the official views of the National Institutes of Health.

Note

Supplementary data for this article are available at Molecular Cancer Therapeutics Online (<http://mct.aacrjournals.org/>).

Received August 30, 2023; revised February 15, 2024; accepted July 10, 2024; published first August 16, 2024.

References

1. Siegel RL, Miller KD, Fuchs HE, Jemal A. Cancer statistics, 2022. CA Cancer J Clin 2022;72:7–33.
2. Conroy T, Hammel P, Hebbar M, Ben Abdelghani M, Wei AC, Raoul JL, et al. FOLFIRINOX or gemcitabine as adjuvant therapy for pancreatic cancer. N Engl J Med 2018;379:2395–406.
3. Royal RE, Levy C, Turner K, Mathur A, Hughes M, Kammula US, et al. Phase 2 trial of single agent Ipilimumab (anti-CTLA-4) for locally advanced or metastatic pancreatic adenocarcinoma. J Immunother 2010;33:828–33.
4. O'Reilly EM, Oh DY, Dhani N, Renouf DJ, Lee MA, Sun W, et al. Durvalumab with or without tremelimumab for patients with metastatic pancreatic ductal adenocarcinoma: a phase 2 randomized clinical trial. JAMA Oncol 2019;5:1431–8.
5. Song J, Durrin LK, Wilkinson TA, Krontiris TG, Chen Y. Identification of a SUMO-binding motif that recognizes SUMO-modified proteins. Proc Natl Acad Sci U S A 2004;101:14373–8.
6. Song J, Zhang Z, Hu W, Chen Y. Small ubiquitin-like modifier (SUMO) recognition of a SUMO binding motif: a reversal of the bound orientation. J Biol Chem 2005;280:40122–9.
7. Yasugi T, Howley PM. Identification of the structural and functional human homolog of the yeast ubiquitin conjugating enzyme UBC9. Nucleic Acids Res 1996;24:2005–10.
8. Kessler JD, Kahle KT, Sun T, Meerbrey KL, Schlabach MR, Schmitt EM, et al. A SUMOylation-dependent transcriptional subprogram is required for Myc-driven tumorigenesis. Science 2012;335:348–53.
9. Golebiowski F, Matic I, Tatham MH, Cole C, Yin Y, Nakamura A, et al. System-wide changes to SUMO modifications in response to heat shock. Sci Signal 2009;2:ra24.
10. Yu B, Swatkoski S, Holly A, Lee LC, Giroux V, Lee CS, et al. Oncogenesis driven by the Ras/Raf pathway requires the SUMO E2 ligase Ubc9. Proc Natl Acad Sci U S A 2015;112:E1724–33.
11. Raghavan S, Winter PS, Navia AW, Williams HL, DenAdel A, Lowder KE, et al. Microenvironment drives cell state, plasticity, and drug response in pancreatic cancer. Cell 2021;184:6119–37.e26.
12. Lightcap ES, Yu P, Grossman S, Song K, Khattar M, Xega K, et al. A small-molecule SUMOylation inhibitor activates antitumor immune responses and potentiates immune therapies in preclinical models. Sci Transl Med 2021;13:eaba7791.
13. Langston SP, Grossman S, England D, Afroze R, Bence N, Bowman D, et al. Discovery of TAK-981, a first-in-class inhibitor of SUMO-activating enzyme for the treatment of cancer. J Med Chem 2021;64:2501–20.
14. Dudek AZ, Juric D, Dowlati A, Vaishampayan U, Assad H, Rodón J, et al. First-in-human phase 1/2 study of the first-in-class SUMO-activating enzyme inhibitor TAK-981 in patients with advanced or metastatic solid tumors or relapsed/refractory lymphoma: phase 1 results [abstract]. In: Society for Immunotherapy of Cancer Annual Meeting 2021; 2021.
15. Ritchie KJ, Malakhov MP, Hetherington CJ, Zhou L, Little MT, Malakhova OA, et al. Dysregulation of protein modification by ISG15 results in brain cell injury. Genes Dev 2002;16:2207–12.
16. Livak KJ, Schmittgen TD. Analysis of relative gene expression data using real-time quantitative PCR and the 2(-Delta Delta C(T)) method. Methods 2001;25: 402–8.
17. Boj SF, Hwang CI, Baker LA, Chio II, Engle DD, Corbo V, et al. Organoid models of human and mouse ductal pancreatic cancer. Cell 2015;160:324–38.
18. Chai MG, Kim-Fuchs C, Angst E, Sloan EK. Bioluminescent orthotopic model of pancreatic cancer progression. J Vis Exp 2013;2013:50395.
19. Narayanan JSS, Ray P, Hayashi T, Whisenant TC, Vicente D, Carson DA, et al. Irreversible electroporation combined with checkpoint blockade and TLR7 stimulation induces antitumor immunity in a murine pancreatic cancer model. Cancer Immunol Res 2019;7:1714–26.

20. Shankara Narayanan JS, Hayashi T, Erdem S, McArdle S, Tiriac H, Ray P, et al. Treatment of pancreatic cancer with irreversible electroporation and intra-tumoral CD40 antibody stimulates systemic immune responses that inhibit liver metastasis in an orthotopic model. *J Immunother Cancer* 2023;11:e006133.
21. Shankara Narayanan JS, Ray P, Naqvi I, White R. A syngeneic pancreatic cancer mouse model to study the effects of irreversible electroporation. *J Vis Exp* 2018;2018:57265.
22. Miller SA, Policastro RA. scProportionTest. San Francisco (CA): Github. 2020. Available from: github.com/rpolicastro/scProportionTest.
23. Peng J, Sun B-F, Chen C-Y, Zhou J-Y, Chen Y-S, Chen H, et al. Single-cell RNA-seq highlights intra-tumoral heterogeneity and malignant progression in pancreatic ductal adenocarcinoma. *Cell Res* 2019;29:725–38.
24. Hafemeister C, Satija R. Normalization and variance stabilization of single-cell RNA-seq data using regularized negative binomial regression. *Genome Biol* 2019;20:296.
25. Park SJ, Yoon BH, Kim SK, Kim SY. GENT2: an updated gene expression database for normal and tumor tissues. *BMC Med Genomics* 2019;12(Suppl 5):101.
26. Lin W, Noel P, Borazanci EH, Lee J, Amini A, Han IW, et al. Single-cell transcriptome analysis of tumor and stromal compartments of pancreatic ductal adenocarcinoma primary tumors and metastatic lesions. *Genome Med* 2020;12:80.
27. Morton JP, Timpson P, Karim SA, Ridgway RA, Athineos D, Doyle B, et al. Mutant p53 drives metastasis and overcomes growth arrest/senescence in pancreatic cancer. *Proc Natl Acad Sci U S A* 2010;107:246–51.
28. Ischenko I, D'Amico S, Rao M, Li J, Hayman MJ, Powers S, et al. KRAS drives immune evasion in a genetic model of pancreatic cancer. *Nat Commun* 2021; 12:1482.
29. Korotkevich G, Sukhov V, Budin N, Shpak B, Artyomov MN, Sergushichev A. Fast gene set enrichment analysis. Cold Spring Harbor (NY): Cold Spring Harbor Laboratory; 2016.
30. Kumar S, Schoonderwoerd MJA, Kroonen JS, de Graaf IJ, Sluijter M, Ruano D, et al. Targeting pancreatic cancer by TAK-981: a SUMOylation inhibitor that activates the immune system and blocks cancer cell cycle progression in a preclinical model. *Gut* 2022;71:2266–83.
31. Ryschich E, Notzel T, Hinz U, Autschbach F, Ferguson J, Simon I, et al. Control of T-cell-mediated immune response by HLA class I in human pancreatic carcinoma. *Clin Cancer* 2005;11:498–504.
32. Zhang L, Li Z, Skrzypczynska KM, Fang Q, Zhang W, O'Brien SA, et al. Single-cell analyses inform mechanisms of myeloid-targeted therapies in colon cancer. *Cell* 2020;181:442–59.e29.
33. Roehle K, Qiang L, Ventre KS, Heid D, Ali LR, Lenehan P, et al. cIAP1/2 antagonism eliminates MHC class I-negative tumors through T cell-dependent reprogramming of mononuclear phagocytes. *Sci Transl Med* 2021;13:ebbf5058.
34. Raghavan S, Winter PS, Navia AW, Williams HL, DenAdel A, Lowder KE, et al. Microenvironment drives cell state, plasticity, and drug response in pancreatic cancer. *Cell* 2021;184:6119–37.e26.
35. Li T, Fu J, Zeng Z, Cohen D, Li J, Chen Q, et al. TIMER2.0 for analysis of tumor-infiltrating immune cells. *Nucleic Acids Res* 2020;48:W509–14.
36. Bronte V, Brandau S, Chen S-H, Colombo MP, Frey AB, Greten TF, et al. Recommendations for myeloid-derived suppressor cell nomenclature and characterization standards. *Nat Commun* 2016;7:12150.
37. Alshetaiwi H, Pervolarakis N, McIntyre LL, Ma D, Nguyen Q, Rath JA, et al. Defining the emergence of myeloid-derived suppressor cells in breast cancer using single-cell transcriptomics. *Sci Immunol* 2020;5:eaay6017.
38. Ohlund D, Elyada E, Tuveson D. Fibroblast heterogeneity in the cancer wound. *J Exp Med* 2014;211:1503–23.
39. Olivares O, Mayers JR, Gouirand V, Torrence ME, Gicquel T, Borge L, et al. Collagen-derived proline promotes pancreatic ductal adenocarcinoma cell survival under nutrient limited conditions. *Nat Commun* 2017;8:16031.
40. Tjomsland V, Niklasson L, Sandstrom P, Borch K, Druid H, Brattahl C, et al. The desmoplastic stroma plays an essential role in the accumulation and modulation of infiltrated immune cells in pancreatic adenocarcinoma. *Clin Dev Immunol* 2011;2011:212810.
41. Ozdemir BC, Pentcheva-Hoang T, Carstens JL, Zheng X, Wu CC, Simpson TR, et al. Depletion of carcinoma-associated fibroblasts and fibrosis induces immunosuppression and accelerates pancreas cancer with reduced survival. *Cancer Cell* 2015;28:831–3.
42. Jin S, Guerrero-Juarez CF, Zhang L, Chang I, Ramos R, Kuan C-H, et al. Inference and analysis of cell-cell communication using CellChat. *Nat Commun* 2021;12:1088.
43. Elyada E, Bolisetty M, Laise P, Flynn WF, Courtois ET, Burkhardt RA, et al. Cross-species single cell analysis of pancreatic ductal adenocarcinoma reveals antigen-presenting cancer-associated fibroblasts. *Cancer Discov* 2019;9: 1102–23.
44. Jin S, Guerrero-Juarez CF, Zhang L, Chang I, Ramos R, Kuan CH, et al. Inference and analysis of cell-cell communication using CellChat. *Nat Commun* 2021;12:1088.
45. Wen T, Barham W, Li Y, Zhang H, Gicobi JK, Hirdler JB, et al. NKG7 is a T-cell-intrinsic therapeutic target for improving antitumor cytotoxicity and cancer immunotherapy. *Cancer Immunol Res* 2022;10:162–81.
46. Tape CJ, Ling S, Dimitriadi M, McMahon KM, Worboys JD, Leong HS, et al. Oncogenic KRAS regulates tumor cell signaling via stromal reciprocation. *Cell* 2016;165:910–20.
47. Dalod M, Chelbi R, Malissen B, Lawrence T. Dendritic cell maturation: functional specialization through signaling specificity and transcriptional programming. *EMBO J* 2014;33:1104–16.
48. Chen Y. A new immuno-oncology target - SUMOylation. *Trends Cancer* 2023; 9:606–8.
49. Steele NG, Carpenter ES, Kemp SB, Sirihorachai VR, The S, Delrosario L, et al. Multimodal mapping of the tumor and peripheral blood immune landscape in human pancreatic cancer. *Nat Cancer* 2020;1:1097–112.
50. Huffman AP, Lin JH, Kim SI, Byrne KT, Vonderheide RH. CCL5 mediates CD40-driven CD4+ T cell tumor infiltration and immunity. *JCI Insight* 2020; 5:e137263.
51. Ding X, Wang A, Ma X, Demarque M, Jin W, Xin H, et al. Protein SUMOylation is required for regulatory T cell expansion and function. *Cell Rep* 2016;16:1055–66.
52. Weitz J, Hurtado de Mendoza T, Tiriac H, Lee J, Sun S, Garg B, et al. An ex-vivo organotypic culture platform for functional interrogation of human appendiceal cancer reveals a prominent and heterogeneous immunological landscape. *Clin Cancer Res* 2022;28:4793–806.
53. Tempe D, Vives E, Brockly F, Brooks H, De Rossi S, Piechaczyk M, et al. SUMOylation of the inducible (c-Fos:c-Jun)/AP-1 transcription complex occurs on target promoters to limit transcriptional activation. *Oncogene* 2014;33: 921–7.
54. Nayak A, Glockner-Pagel J, Vaeth M, Schumann JE, Buttmann M, Bopp T, et al. Sumoylation of the transcription factor NFATc1 leads to its subnuclear relocation and interleukin-2 repression by histone deacetylase. *J Biol Chem* 2009;284:10935–46.
55. Xiao Y, Qureischi M, Dietz L, Vaeth M, Vallabhapurapu SD, Klein-Hessling S, et al. Lack of NFATc1 SUMOylation prevents autoimmunity and alloreactivity. *J Exp Med* 2021;218:e20181853.